

Iridium-platinum alloy nanoparticles: Composition-dependent electrocatalytic activity for formic acid oxidation†

Wei Chen^{*a} and Shaowei Chen^{*b}

Received 6th January 2011, Accepted 3rd May 2011

DOI: 10.1039/c1jm00077b

$\text{Ir}_x\text{Pt}_{100-x}$ alloy nanoparticles with varied compositions ($x = 100, 75, 67, 50, 34,$ and 0) were synthesized by a thermolytic process at varied ratios of the IrCl_3 and PtCl_2 precursors. High-resolution transmission electron microscopic (HRTEM) measurements showed that the nanoparticles all exhibited well-defined crystalline structures with the average core diameters around 2 nm; and the elemental compositions were determined by X-ray photoelectron spectroscopic (XPS) measurements. The electrocatalytic activities of the $\text{Ir}_x\text{Pt}_{100-x}$ nanoparticles toward formic acid oxidation were then examined by electrochemical measurements, including cyclic voltammetry (CV), chronoamperometry, and electrochemical impedance spectroscopy (EIS). In the CV studies, it was found that both the current density of formic acid oxidation and the tolerance to CO poisoning were strongly dependent on the composition of the iridium-platinum alloy nanoparticles, with the best performance found with the $\text{Ir}_{50}\text{Pt}_{50}$ nanoparticles. Due to heavy CO poisoning, Pt nanoparticles exhibited the lowest catalytic performance among the series of nanoparticles (excluding Ir nanoparticles). The $\text{Ir}_{50}\text{Pt}_{50}$ nanoparticles also showed the maximum current density and stability in chronoamperometric measurements. Consistent results were obtained in electrochemical impedance spectroscopic studies of the electron transfer kinetics involved. Notably, of all the nanoparticle electrocatalysts, an inductive component, *i.e.* negative impedance, was observed in the potential windows where CO was removed by electro-oxidation; and the charge transfer resistance was found to be the lowest with the $\text{Ir}_{50}\text{Pt}_{50}$ nanoparticles. Based on the current density and peak potential of formic acid oxidation, the ratio of the anodic peak current density to the cathodic peak current density measured in CV studies, the stability manifested in chronoamperometric measurements and the tolerance to CO poisoning displayed in EIS measurements, the electrocatalytic performance of the IrPt alloy nanoparticles was found to decrease in the order of $\text{Ir}_{50}\text{Pt}_{50} > \text{Ir}_{67}\text{Pt}_{33} > \text{Ir}_{75}\text{Pt}_{25} > \text{Ir}_{34}\text{Pt}_{66} > \text{Pt}$. That is, among the series of IrPt alloy nanoparticles, the sample with the Ir/Pt atomic ratio of 1 : 1 showed the highest electrocatalytic activity towards formic acid oxidation, which might be ascribed to the bifunctional reaction mechanism of bimetallic alloy electrocatalysts.

Introduction

In the past decades, research on direct liquid fuel cells has attracted considerable attention due to the shrinking reserves of fossil fuels and the increasing worldwide energy demand.¹⁻³ A variety of small organic molecules have been identified as potential fuels, such as methanol, ethanol, and formic acid. Among these, much research has been carried out to examine the electro-

oxidation of methanol. However, direct methanol fuel cells (DMFCs) have been found to exhibit several notable disadvantages, such as high crossover through the polymer membrane, toxicity and hence possible environmental problems, complicated reaction pathways and sluggish anodic oxidation kinetics. In recent years, formic acid has been proposed and recognized as an attractive substituent for direct formic acid fuel cells (DFAFCs). In comparison with methanol, formic acid has several advantages.⁴⁻⁶ Firstly, formic acid has a high theoretical open circuit voltage (1.45 V). Secondly, formic acid has a lower rate of crossover through the Nafion membrane than methanol, which means that DFAFCs may have a higher fuel concentration than DMFCs. Thirdly, formic acid is not toxic and inflammable at room temperature and thus it is safe in handling and distribution.

Up to now, membrane materials and electrocatalysts on both anode and cathode are the main limiting factors in the

^aState Key Laboratory of Electroanalytical Chemistry, Changchun Institute of Applied Chemistry, Chinese Academy of Sciences, Changchun, Jilin, 130022, China. E-mail: weichen@ciac.jl.cn

^bDepartment of Chemistry and Biochemistry, University of California, Santa Cruz, California, 95064, USA. E-mail: shaowei@ucsc.edu

† Electronic supplementary information (ESI) available: UV-vis absorption spectra and additional electrochemical impedance spectra of the IrPt nanoparticles. See DOI: 10.1039/c1jm00077b

determination of the fuel cell performance. As for anodic electrocatalysts, platinum and Pt-based alloys have been widely used and shown the highest catalytic activity for the electro-oxidation of methanol and formic acid.^{7–11} It has been generally accepted that the anodic oxidation of HCOOH proceeds *via* the so-called dual path mechanism, that is, indirect path (adsorbed poisonous CO intermediate) and direct path (non-CO reactive intermediate).^{12,13} It is well-known that the formation of strongly adsorbed CO leads to the self-poisoning of the electrocatalysts. In comparison with pure platinum catalysts, alloys of platinum with other transition metals display an improved activity due to the bifunctional mechanism, in which the second metals facilitate the dissociation of water to form adsorbed OH species, which then oxidize CO species adsorbed on neighboring Pt sites to CO₂.^{3,14–16}

In recent years, with the development of nanoscale functional materials, a vast number of nanoparticles, especially metal alloy nanoparticles, have been prepared and used as electrocatalysts due to the unique catalytic properties in comparison with the corresponding bulk counterparts.^{11,17–26} In the previous studies of metal nanoparticle catalysts, it has been found that the electrocatalytic activity depends strongly on the particle dimensions, since the accessible surface sites and electronic properties of metal nanoparticles both vary as a function of the particle size.^{27–30} For alloy nanoparticles, in addition to particle dimensions, the composition of the particles also acts as a very important parameter in the manipulation of their catalytic activity. Such composition effects have, for instance, been observed and investigated in the electro-oxidation of methanol and formic acid by PtRu and FePt alloy nanoparticle catalysts, where it was found that the optimal catalysts corresponded to a composition of 1 : 1 atomic ratio of ruthenium or iron to platinum.^{31–33}

Iridium (Ir) is an important transition-metal catalyst for alkene, aldehyde and ketone hydrogenation.^{34–36} Methanol oxidation on iridium metal has been studied, and yet Ir shows rather poor catalytic activity in comparison with Pt, Pd or Rh metals.^{37,38} However, oxygen species on iridium can be formed at relatively low potentials,³⁷ which may be exploited for the improved catalytic performance of IrPt alloys in formic acid oxidation. In fact, several recent studies have showed that binary or ternary Pt alloys with Ir exhibited excellent catalytic activities as anode electrocatalysts for methanol or formic acid electro-oxidation^{39–45} and as cathode electrocatalysts for oxygen reduction.^{46–48} For example, carbon supported Pt₂₅(Ru-Ir)₇₅ nanoparticles prepared by a sol-gel process exhibited approximately 93 and 13 times higher current density of methanol oxidation at +0.5 V than that on the Pt/C and Pt₇₅Ru₂₅/C commercial catalysts, respectively.⁴⁹ However, so far there have been a limited number of studies that focus on the compositional effect of unsupported IrPt alloy nanoparticles, with the particle size smaller than 5 nm, on their electrocatalytic activity.

In the present study, Ir_xPt_{100-x} ($x = 100$ to 0) binary alloy nanoparticles with a core diameter of about 2 nm were prepared by a simple procedure based on thermolysis at varied ratios of the precursors of IrCl₃ and PtCl₂. The structures of the resulting nanoparticles were characterized by X-ray photoelectron spectroscopy (XPS), high-resolution transmission electron microscopy (HRTEM), and UV-visible spectroscopy. The electrocatalytic activities of these alloy particles in formic acid oxidation were then examined by voltammetric and

electrochemical impedance measurements. The electrocatalytic activities were compared on the basis of (steady-state) current density and tolerance to CO adsorption in formic acid oxidation. It was found that within the present experimental context, the Ir₅₀Pt₅₀ nanoparticles exhibited the best performance and therefore the optimal composition for formic acid electro-oxidation.

Experimental section

Chemicals

Iridium chloride (IrCl₃, ACROS), platinum chloride (PtCl₂, ACROS), 1,2-propanediol (ACROS), sodium acetate trihydrate (NaAc·3H₂O, MC&B), 1-octanethiol (C8SH, 97%, ACROS), formic acid (HCOOH, ACROS, 99%) and perchloric acid (HClO₄, Fisher, 99%) were used as received. All solvents were obtained from typical commercial sources and used without further treatment. Water was supplied by a Barnstead Nanopure water system (18.3 MΩ·cm). In electrochemical studies, all solutions were deaerated by bubbling ultrahigh-purity N₂ for 20 min and protected with a nitrogen atmosphere during the entire experimental procedure.

Preparation of Ir_xPt_{100-x} nanoparticles

Ir ($x = 100$) and Pt ($x = 0$) nanoparticles were synthesized by the thermolytic reduction of iridium chloride or platinum chloride in 1,2-propanediol that was used previously in the preparation of ruthenium nanoparticles.^{50–53} For the synthesis of Ir_xPt_{100-x} alloy nanoparticles, the total amount of the precursors (IrCl₃ and PtCl₂) was kept constant at 1 mmol, and the metal salts were co-reduced by 1,2-propanediol. Briefly, x mmol of IrCl₃ and $1 - x$ mmol PtCl₂ together with 2 mmol of NaAc were dissolved in 200 mL of 1,2-propanediol. The mixed solution was heated at 165 °C for 15 min under vigorous stirring. During the reaction, the color of the solution was found to change to dark brown indicating the formation of Ir_xPt_{100-x} alloy nanoparticles. After the colloid solution was cooled down to room temperature, octanethiol dissolved in toluene with three-fold molar excess as compared to the metal salt was added into the solution under magnetic stirring overnight. A dark brown color appeared in the toluene phase whereas the diol phase became colorless, signifying the extraction of the particles from the diol phase to the toluene phase. Such a phase transfer of Ir_xPt_{100-x} nanoparticles from the hydrophilic medium (diol) to the hydrophobic phase (toluene) indicated that the Ir_xPt_{100-x} particles were now capped with a hydrophobic surfactant layer (C8SH). With the addition of 20 mL of Nanopure water to further separate the two phases, the toluene portion was collected and dried at reduced pressure. Methanol was then used to remove excessive ligands, affording purified nanoparticles. Like alkanethiolate-protected Au, Pd, Ag and other metal nanoparticles, the resulting Ir, Pt and Ir_xPt_{100-x} nanoparticles were found to be soluble in non-polar solvents, such as dichloromethane, hexane, but not in polar solvent such as alcohols and water.

Spectroscopies

The composition of the particles was evaluated by X-ray photoelectron spectroscopy (XPS) measurements. The XPS

spectra were collected with a Phi 5400 XPS surface analysis system equipped with a Mg-K α line (1253.6 eV, 300 W) as the X-ray source at a base pressure of 8×10^{-9} Torr. The particle core diameter was measured with a Philips CM200/FEG high-resolution transmission electron microscope (HRTEM). The samples were prepared by casting a drop of the particle solution (~ 1 mg mL $^{-1}$) in dichloromethane onto a 200-mesh carbon-coated copper grid. UV-vis spectroscopic studies were performed with an ATI Unicam UV4 spectrometer using a 1-cm quartz cuvette with a resolution of 2 nm.

Electrochemistry

Voltammetric measurements were carried out with a CHI 440 electrochemical workstation. A polycrystalline gold disk electrode (sealed in a glass tubing) was used as the working electrode, and a Ag/AgCl (in 3 M NaCl, aq) and a Pt coil were used as the reference and counter electrodes, respectively. Prior to use, the gold electrode was polished with alumina slurries of 0.05 μ m and then cleansed by sonication in 0.1 M HNO $_3$, H $_2$ SO $_4$ and Nanopure water successively. To prepare electrodes for formic acid oxidation, 4 μ L of the prepared nanoparticles dissolved in CH $_2$ Cl $_2$ (1 mg mL $^{-1}$) were then dropcast onto the clean Au electrode surface by a Hamilton microlitre syringe. The particle film was dried by a gentle stream of ultrahigh-purity nitrogen for *ca.* 2 min. The organic protecting ligands were then removed by oxidation in an ultraviolet ozone (UVO) chamber (Jelight Company, Inc., Model 42) for about 15 min; and the corresponding electrode was denoted as Ir $_x$ Pt $_{100-x}$ /Au. Prior to data collection, the electrolyte solution was deaerated by bubbling ultrahigh-purity N $_2$ for at least 20 min and blanketed with a nitrogen atmosphere during the entire experimental procedure.

Results and discussion

Structural characterization

In the present study, the composition of the IrPt nanoparticles was controlled by varying the ratio of the IrCl $_3$ and PtCl $_2$ precursors during nanoparticle synthesis. X-ray photoelectron spectroscopic (XPS) measurements were performed to determine the chemical states as well as the relative contents of the iridium and platinum elements in the nanoparticles. Fig. 1 shows the XPS spectra of the series of Ir $_x$ Pt $_{100-x}$ nanoparticles in the Pt 4f and Ir 4f region. From curve (a), it can be seen that Pt nanoparticles exhibited two energy bands at 71.6 and 74.8 eV, corresponding to the Pt 4f $_{7/2}$ and Pt 4f $_{5/2}$ core electrons, respectively. The positions of these two peaks and the binding energy difference ($\Delta E = 3.2$ eV) between the doublet strongly indicate the existence of metallic Pt(0).⁵⁴ For the Ir $_x$ Pt $_{100-x}$ alloy nanoparticles (curves (b) to (e)), the Pt 4f $_{7/2}$ and Pt 4f $_{5/2}$ core electrons were found at around 71.3 and 74.6 eV, respectively, exhibiting a modest downshift of about 0.3 and 0.2 eV as compared to those of Pt nanoparticles (curve (a)). In the energy range of 58 to 68 eV, two bands at 60.9 and 63.9 eV in curve (f) can be observed with Ir nanoparticles, which are the typical values of the 4f $_{7/2}$ and 4f $_{5/2}$ electrons of metallic Ir (0);⁵⁵ whereas in the Ir $_x$ Pt $_{100-x}$ alloy nanoparticles (curves (b) to (e)) these two peaks were found to upshift slightly to 61.0 and 64.0 eV, respectively. Similar observations were reported in previous studies of Ir-Pt nanostructured

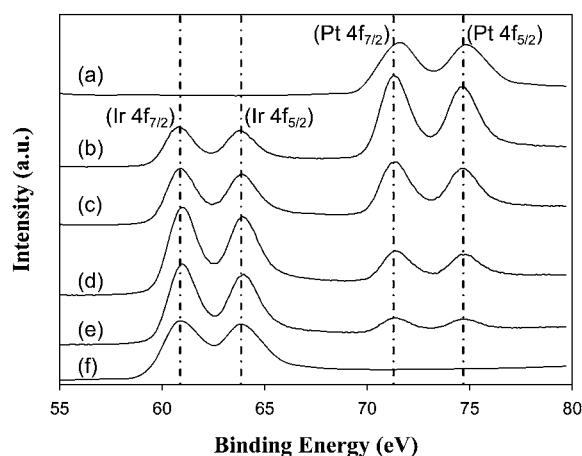


Fig. 1 X-ray photoelectron spectra of the Pt 4f and Ir 4f core electrons of the Ir $_x$ Pt $_{100-x}$ nanoparticles ($x = 0$ to 100).

materials,⁵⁶ where the Pt 4f $_{7/2}$ and 4f $_{5/2}$ doublets were found at 71.4 and 74.7 eV, and the Ir 4f $_{7/2}$ and 4f $_{5/2}$ electrons at 60.9 and 63.6 eV, respectively. The decrease of the binding energy of Pt 4f electrons and the concurrent increase of those of Ir 4f electrons in the Ir $_x$ Pt $_{100-x}$ alloy nanoparticles may be ascribed to the electronic interactions between the Pt and Ir atomic orbitals, leading to (partial) electron transfer from Ir to Pt. The XPS results also strongly suggest the formation of Ir-Pt alloys, as such a variation of the binding energy has also been observed with other Pt-based alloy nanoparticles.^{57,58} The intensities of the XPS signals of the Pt and Ir 4f electrons were then used to evaluate the elemental compositions of the bimetallic nanoparticles. From curves (b) to (e) in Fig. 1, the compositions of the as-produced Ir $_x$ Pt $_{100-x}$ alloy nanoparticles were determined to be Ir $_{34}$ Pt $_{66}$, Ir $_{50}$ Pt $_{50}$, Ir $_{67}$ Pt $_{33}$, and Ir $_{75}$ Pt $_{25}$, as summarized in Table 1.

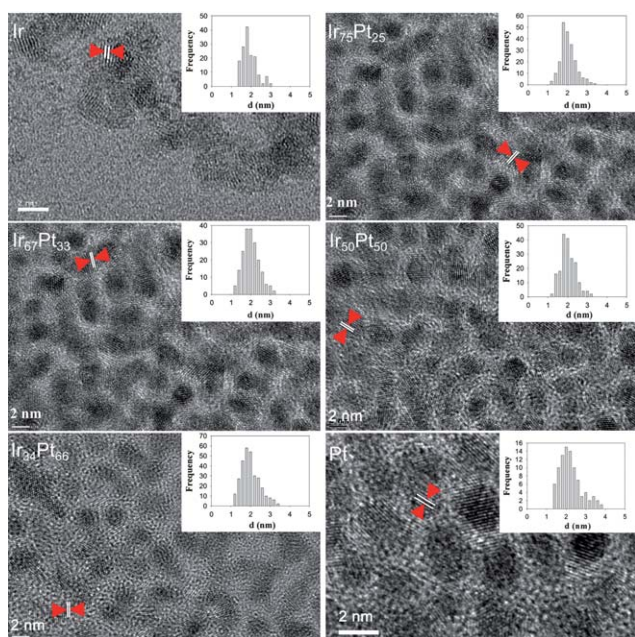
The formation of Ir $_x$ Pt $_{100-x}$ alloy nanoparticles was also characterized by UV-vis measurements. It has been well-known that transition-metal nanoparticles exhibit unique optical characteristics with an exponential-decay absorption profile with increasing wavelength, as predicted by the Mie theory.⁵⁹ Fig. S1 (Electronic Supplementary Information, ESI †) depicts the UV-vis absorption spectra of the IrCl $_3$ and PtCl $_2$ precursors as well as the series of Ir $_x$ Pt $_{100-x}$ nanoparticles. It can be seen that IrCl $_3$ exhibits two broad absorption peaks at about 440 and 490 nm, and PtCl $_2$ shows an absorption band at 261 nm, which can be ascribed to the corresponding metal (Pt, Ir)-ligand (M-L) transitions. After thermolytic reduction by 1,2-propanediol, these peaks disappeared and the absorption curves demonstrated an exponential decay profile regardless of the nanoparticle composition, consistent with the formation of IrPt alloy nanoparticles.

The morphology and crystalline structures of the Ir $_x$ Pt $_{100-x}$ alloy nanoparticles were then examined by high-resolution transmission electron microscopic (HRTEM) measurements. Fig. 2 shows a representative HRTEM micrograph for each of the Ir $_x$ Pt $_{100-x}$ nanoparticles ($x = 0$ to 100). It can be seen that all nanoparticles, roughly in spherical shapes, were well dispersed without apparent aggregation. From the particle core size histograms (figure insets), the nanoparticles all exhibited a rather narrow size distribution in the range of 1 to 4 nm with an average core diameter close to 2.0 nm, which was summarized in Table 1.

Table 1 Average core size, size distribution and composition of the $\text{Ir}_x\text{Pt}_{100-x}$ nanoparticles

Nanoparticle	(a)	(b)	(c)	(d)	(e)	(f)
Core size (nm) ^a	2.21 ± 0.50	2.00 ± 0.31	2.03 ± 0.19	2.02 ± 0.24	2.04 ± 0.21	1.91 ± 0.37
Core composition ^b	Pt	$\text{Ir}_{34}\text{Pt}_{66}$	$\text{Ir}_{50}\text{Pt}_{50}$	$\text{Ir}_{67}\text{Pt}_{33}$	$\text{Ir}_{75}\text{Pt}_{25}$	Ir

^a Particle core sizes were derived from HRTEM measurements as exemplified in Fig. 2. ^b Particle core compositions were determined by XPS analysis as depicted in Fig. 1.

**Fig. 2** Representative high-resolution TEM micrographs of the $\text{Ir}_x\text{Pt}_{100-x}$ nanoparticles. The scale bars are all 2 nm. The insets show the corresponding particle core size histograms.

In other words, the particle diameter remained virtually invariant with the composition of the $\text{Ir}_x\text{Pt}_{100-x}$ nanoparticles changed from $x = 100$ to 0. Moreover, closer examinations of the HRTEM micrographs show that the nanoparticles all exhibited well-defined crystalline lattice fringes (red arrows and white lines). In fact, the interplanar spacing was found to be approximately 0.22 nm for Ir nanoparticles and 0.23 nm for other nanoparticles, in agreement with the Ir (111) and Pt (111) lattice planes, respectively. Since the obtained $\text{Ir}_x\text{Pt}_{100-x}$ nanoparticles exhibited rather uniform shape and size, their electrocatalytic activity in the electro-oxidation of formic acid can then be correlated to the particle composition, as manifested below.

Cyclic voltammetry

The electrochemical properties of the $\text{Ir}_x\text{Pt}_{100-x}$ nanoparticles were then evaluated by cyclic voltammetric measurements in an acid electrolyte. Fig. 3 shows the steady-state cyclic voltammograms of the resulting $\text{Ir}_x\text{Pt}_{100-x}$ ($x = 100, 75, 67, 50, 34$ and 0) nanoparticles deposited onto a Au electrode (with the organic components removed by UVO treatment) in 0.1 M HClO_4 at a potential sweep rate of 0.1 V s^{-1} . From the voltammetric response of Ir nanoparticles, it can be seen that there are two pairs of anodic and cathodic current peaks at around +0.62 and

+0.88 V and the voltammetric profile is symmetrical about the potential axis. The symmetrical current peaks have generally been attributed to the reversible chemisorption of oxygen-containing species on iridium metal surfaces, similar to those observed previously with Ir metal electrodes.^{60,61} With the increase of the Pt content in the $\text{Ir}_x\text{Pt}_{100-x}$ nanoparticles, the voltammetric features from iridium diminished whereas those from Pt became progressively prominent. In particular, for the $\text{Ir}_{34}\text{Pt}_{66}$ and Pt samples, two pairs of well-defined current peaks can be observed at -0.15 and -0.05 V, which are ascribed to the hydrogen adsorption and desorption on Pt surfaces. In addition, in the positive potential scan, Pt oxides were formed at potentials more positive than +0.48 V; and in the reverse scan, the current from the reduction of Pt oxides can be seen at around +0.53 V. These apparent voltammetric features from Pt and Ir indicate that the prepared electrodes are electrochemically active after the removal of the organic protecting ligands by UVO treatment. It should be noted that in previous electrochemical studies, Pt-based metal alloys (*e.g.*, with Fe, Co, Ni, *etc*) typically exhibit voltammetric features that are consistent with the formation of a platinum skin after electrochemical cycling in acid electrolytes.^{16,31,62-64} In the present study, the voltammetric characteristics of Pt became increasingly prominent with increasing Pt content in the $\text{Ir}_x\text{Pt}_{100-x}$ nanoparticles, suggesting that the $\text{Ir}_x\text{Pt}_{100-x}$ nanoparticles are highly stable during the electrochemical cycling and thus provide stable surface structures where the effect of nanoparticle composition on the electrocatalytic activity toward formic acid oxidation can be examined, as detailed below.

Electro-oxidation of formic acid

Fig. 4 depicts the steady-state cyclic voltammograms of formic acid oxidation with the above $\text{Ir}_x\text{Pt}_{100-x}/\text{Au}$ electrodes in 0.1 M $\text{HCOOH} + 0.1 \text{ M HClO}_4$ at a potential scan rate of 0.1 V/s . Note that the voltammetric currents have been normalized to the electrochemically active surface area of the respective electrode that was estimated by using the voltammograms presented in Fig. 3 and assuming $210 \mu\text{C cm}^{-2}$ for the hydrogen desorption on Pt surfaces (for Ir nanoparticles, the geometric area of the Au substrate was used). From Fig. 4, it can be seen that no obvious features of HCOOH oxidation were observed with the Ir nanoparticles, indicating poor electrocatalytic activity of Ir metal for formic acid oxidation. With the presence of Pt in the nanoparticles, the electrocatalytic activity was enhanced markedly, which exhibited strong dependence on the composition of the nanoparticles. For instance, with the $\text{Ir}_{75}\text{Pt}_{25}$ nanoparticles, two voltammetric peaks emerged at +0.32 and +0.65 V in the positive potential scan. The first current peak is ascribed to the direct

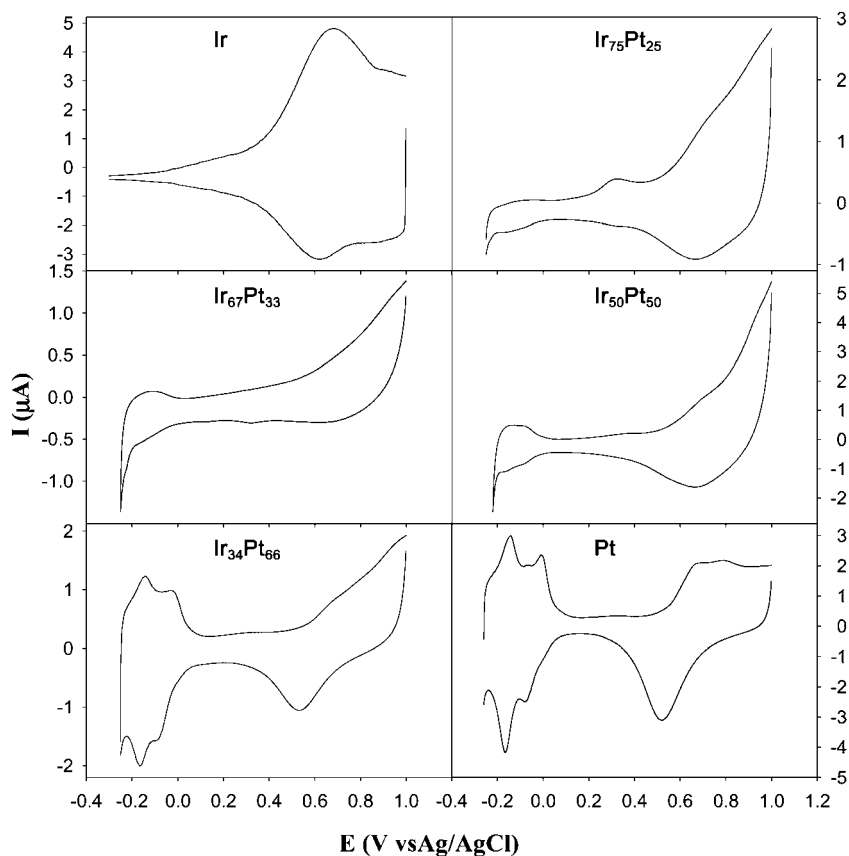


Fig. 3 Cyclic voltammograms of the $\text{Ir}_x\text{Pt}_{100-x}/\text{Au}$ electrodes in 0.1 M HClO_4 . Potential scan rate 0.1 V/s. Gold electrode surface area 0.3 mm^2 .

oxidation of formic acid on the active particle surfaces where no poisonous intermediates (mainly CO) were adsorbed. The peak at the more positive potential can be ascribed to the oxidation of adsorbed CO which arose from the dissociation of formic acid at low potentials, as well as the oxidation of HCOOH at the recovered surface active sites after CO removal. In the reverse scan, an oxidation peak with a much higher current density than those in the anodic scan can be observed, which is attributed to the direct oxidation of HCOOH on the entire particle surface free of CO poisoning. Similar features were observed with other $\text{Ir}_x\text{Pt}_{100-x}$ nanoparticles ($x = 67, 34,$ and 0) except $\text{Ir}_{50}\text{Pt}_{50}$ where the voltammetric features are drastically different. At the $\text{Ir}_{50}\text{Pt}_{50}/\text{Au}$ electrode. Firstly, only one major current peak at $+0.26$ V can be observed along with a negligible shoulder around $+0.67$ V. The presence of a tiny oxidation current peak at the more positive potential suggests that there was little CO poisoning of the $\text{Ir}_{50}\text{Pt}_{50}$ nanoparticles in formic acid oxidation. Secondly, by comparing the peak current density of HCOOH oxidation at around $+0.27$ V on all $\text{Ir}_x\text{Pt}_{100-x}$ nanoparticles (Fig. 5, panel a), the largest current density was observed at the $\text{Ir}_{50}\text{Pt}_{50}/\text{Au}$ electrode, indicating the highest electrocatalytic activity of $\text{Ir}_{50}\text{Pt}_{50}$ among the series of $\text{Ir}_x\text{Pt}_{100-x}$ alloy nanoparticles. Thirdly, $\text{Ir}_{50}\text{Pt}_{50}$ exhibits the highest ratio of the current density of the first anodic oxidation peak (J_a) to the cathodic peak (J_c), suggesting the best tolerance among the series to CO poisoning. As depicted in Fig. 5 (b), the J_a/J_c ratios are found to be 0.51, 0.65, 1.84, 0.37, and 0.29, respectively, for $\text{Ir}_{75}\text{Pt}_{25}$,

$\text{Ir}_{67}\text{Pt}_{33}$, $\text{Ir}_{50}\text{Pt}_{50}$, $\text{Ir}_{34}\text{Pt}_{66}$, and Pt. In fact, as depicted in Fig. 5, both peak current density of formic acid oxidation and the J_a/J_c ratios exhibit a volcano-shaped variation with particle compositions, with the maximum at $\text{Ir}_{50}\text{Pt}_{50}$, suggesting that $x = 50$ might represent the optimal composition of the alloy nanoparticles in formic acid electro-oxidation. Moreover, in comparison with the performance of pure Pt nanoparticles, it can be seen that alloying with Ir leads to drastic enhancement of the electrocatalytic activity.

Furthermore, in comparison to other Pt-based nanoparticles, the $\text{Ir}_x\text{Pt}_{100-x}$ nanoparticles described above exhibit higher electrocatalytic activity. For instance, the onset potential for HCOOH oxidation at PtRu nanoparticles and commercial PtRu catalysts has been reported to be around 0.00 V.²¹ However, in the present study with the $\text{Ir}_x\text{Pt}_{100-x}$ nanoparticles, the onset potentials were found to shift negatively to around -0.10 to -0.15 V (Fig. 4). In addition, the current density at the $\text{Ir}_x\text{Pt}_{100-x}$ nanoparticles (e.g., the anodic peak current density of 17.04 mA cm^{-2} at $\text{Ir}_{50}\text{Pt}_{50}$) is much higher than those observed with homemade (1.35 mA cm^{-2}) and commercial PtRu (0.86 mA cm^{-2}) electrocatalysts. Since onset potential and current density are two important parameters in the quantitative evaluation of the activities of electrocatalysts, the lower onset potentials and larger current densities of the nanometre-sized $\text{Ir}_x\text{Pt}_{100-x}$ nanoparticles suggest that the as-prepared IrPt nanoparticles (especially $\text{Ir}_{50}\text{Pt}_{50}$) may serve as promising anode electrocatalysts in direct formic acid fuel cells.

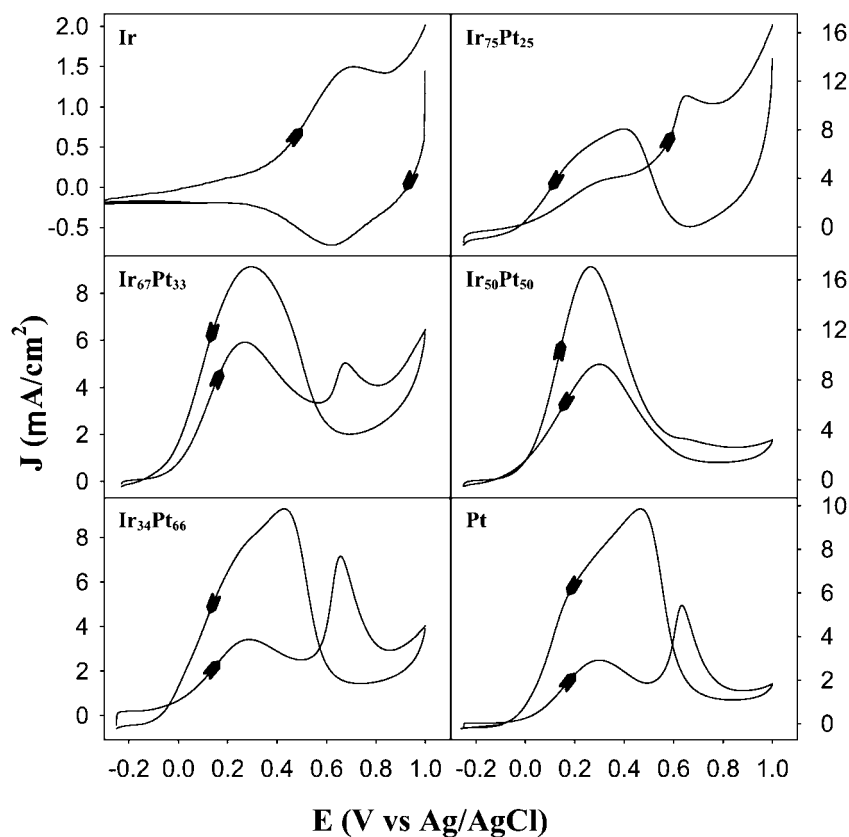


Fig. 4 Cyclic voltammograms of the $\text{Ir}_x\text{Pt}_{100-x}/\text{Au}$ electrodes in 0.1 M $\text{HCOOH} + 0.1 \text{ M HClO}_4$. Potential scan rates 0.1 V/s. Gold electrode surface area 0.3 mm^2 .

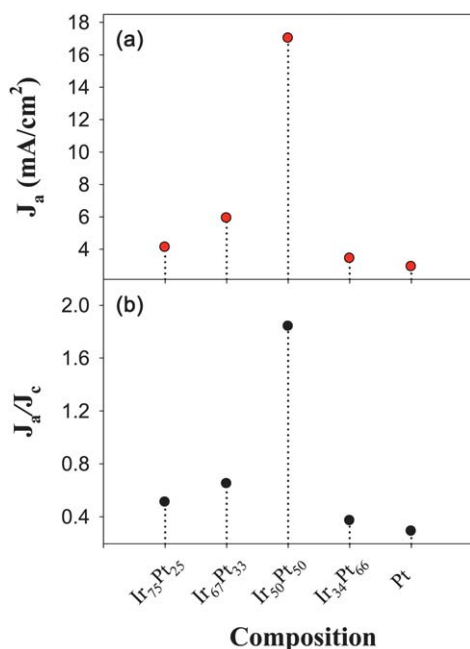


Fig. 5 (a) Current density of the first anodic oxidation peak and (b) ratio of the first anodic peak and cathodic peak currents for the direct oxidation of formic acid at varied nanoparticle compositions. Results were obtained from Fig. 4.

The long-term stability of the catalytic performance was then evaluated by chronoamperometric measurements where the current density-time (J - t) curves at fixed potentials were recorded. Fig. 6 shows the chronoamperometric curves of the $\text{Ir}_x\text{Pt}_{100-x}/\text{Au}$ electrodes in 0.1 M $\text{HCOOH} + 0.1 \text{ M HClO}_4$ by stepping the potential from -0.20 V to (a) 0.0, (b) $+0.26 \text{ V}$, and (c) $+0.50 \text{ V}$, corresponding to the onset, peak and end of the direct oxidation of formic acid, as manifested in Fig. 4. The initial high current density arose from the combined contributions of double-layer charging and formic acid oxidation at the active sites. With the poisoning of CO-like intermediates, the current density decayed rapidly in the first few seconds and attained a steady state thereafter. From the J - t curves in Fig. 6, it can be seen that $\text{Ir}_{50}\text{Pt}_{50}$ nanoparticles exhibited the highest steady-state oxidation current density at all potentials. For instance, when the electrode potential was stepped to the peak potential ($+0.26 \text{ V}$, panel (b)), the steady-state current densities for $\text{Ir}_{75}\text{Pt}_{25}$, $\text{Ir}_{67}\text{Pt}_{33}$, $\text{Ir}_{50}\text{Pt}_{50}$, $\text{Ir}_{34}\text{Pt}_{66}$ nanoparticles were observed at 1.19, 1.84, 2.30, 1.33 mA cm^{-2} , respectively, which were all greater than that of the Pt nanoparticles (1.05 mA cm^{-2}). These results show that among the series, $\text{Ir}_{50}\text{Pt}_{50}$ alloy nanoparticles exhibited the highest catalytic activity and stability in formic acid oxidation, consistent with the voltammetric measurements (Fig. 4 and 5). Similar results were reported in a previous study, where Yi *et al.*⁴³ examined the activity of Ti-supported nanoporous bimetallic Pt-Ir electrocatalysts for formic acid oxidation, and found that for the $\text{Pt}_{59}\text{Ir}_{49}$, $\text{Pt}_{44}\text{Ir}_{56}$ and $\text{Pt}_{22}\text{Ir}_{78}$

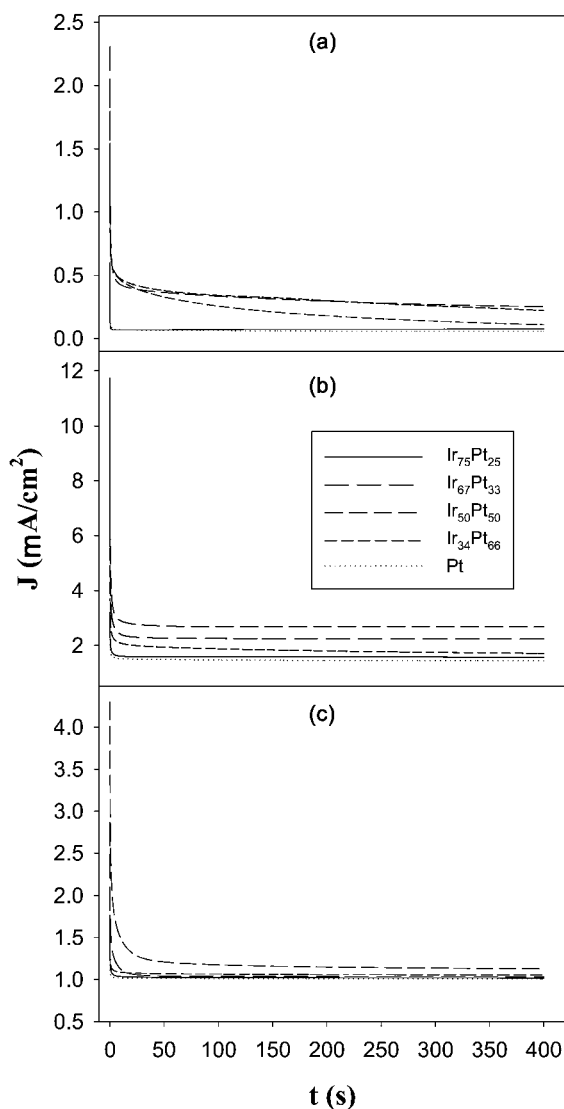


Fig. 6 Chronoamperometric curves in 0.1 M HCOOH + 0.1 M HClO₄ at different Ir_xPt_{100-x}/Au electrodes (shown in the figure legends) where the potential was stepped from -0.2 V to (a) 0.0 V, (b) +0.26 V, and (c) +0.50 V.

nanoparticles (>100 nm), Pt₄₄Ir₅₆/Ti exhibited the best electrocatalytic performance.

Electrochemical impedance spectroscopy

The electron transfer kinetics of formic acid oxidation on the series of Ir_xPt_{100-x} nanoparticles was then elaborated with electrochemical impedance spectroscopic (EIS) measurements. Fig. 7 depicts the representative Nyquist complex-plane impedance spectra of (a) Ir₅₀Pt₅₀/Au and (b) Pt/Au electrodes in 0.1 M HCOOH + 0.1 M HClO₄ at selected electrode potentials (shown as figure legends). From panel (a), it can be seen that at the Ir₅₀Pt₅₀/Au electrode, within the potential range of -0.20 to +0.20 V, the diameter of the impedance arc increased slightly with increasing potential, most probably due to the accumulation of CO on the nanoparticle surface that impeded the electron transfer kinetics. With a further increase of the electrode

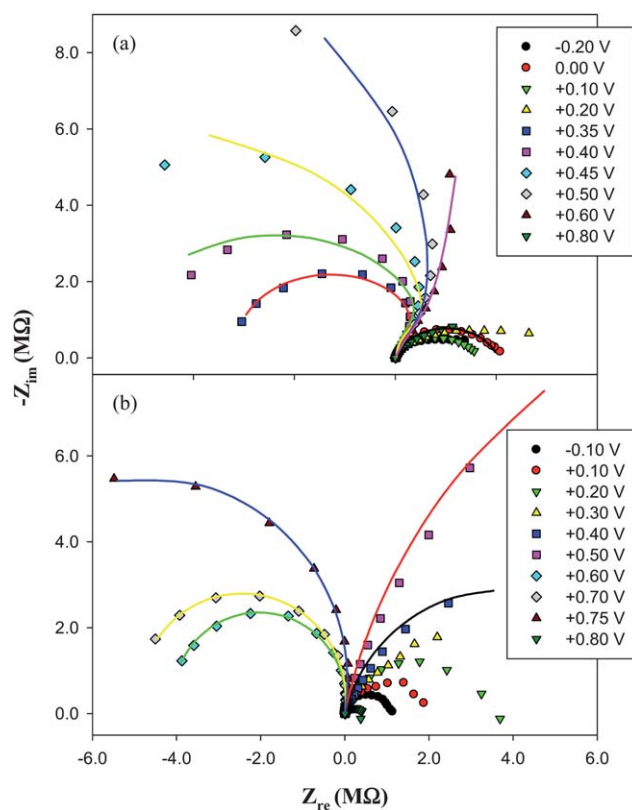


Fig. 7 Complex plane (Nyquist) impedance plots of the (a) Ir₅₀Pt₅₀/Au and (b) Pt/Au electrodes in 0.1 M HCOOH + 0.1 M HClO₄ at various electrode potentials (shown as figure legends). Lines are representative simulations based on the equivalent circuits shown in Fig. 8 (a) and (b).

potential from +0.25 to +0.50 V, the impedance arcs started to appear in the second quadrant instead of the conventional first one. Negative faradaic impedance has also been observed in the oxidation of small organic fuels at other electrocatalysts,^{8,42-44,65-67} which was ascribed to the oxidative removal of the adsorbed CO intermediates with the formation of chemisorbed hydroxyl species within the potential range. Note that in the voltammetric measurements (Fig. 4), the oxidation current peak appeared in the same potential range of +0.25 to +0.50 V. At more positive potentials (> +0.60 V), the impedance arcs returned to the normal first quadrant and the diameter of the arcs decreased with increasing electrode potential, suggesting the diminishment of charge-transfer resistance.

For comparison, the impedance spectra on the Pt/Au electrode at different electrode potentials were shown in Fig. 7 (b). One can see that the diameter of the impedance arcs increased with increasing potential within a wider potential range of -0.20 V to +0.50 V, suggesting that the accumulation of CO on the electrode surface occurred within a much larger potential regime than that at the Ir₅₀Pt₅₀/Au electrode (panel (a)). At potentials more positively than +0.5 V, the impedance arcs appeared in the second quadrant, in accord with the voltammetric response where CO started to be oxidized at these potentials (Fig. 4). With a further increase of the electrode potentials (> +0.8 V), the impedance plots also returned to the first quadrant.

Similar impedance features were observed with other $\text{Ir}_x\text{Pt}_{100-x}$ nanoparticle catalysts (Figures S2–S4, ESI), although the appearance of negative impedance started to occur at somewhat different potentials, as reflected by the variation of the charge transfer resistance (R_{CT}) with electrode potentials (Fig. 8). Note that R_{CT} was quantified by fitting the impedance arcs with the equivalent circuits that were depicted in panels (a) and (b), where R_{S} is the solution resistance, CPE (constant-phase element) and R_{CT} are the double-layer capacitance and charge-transfer resistance, respectively, and C_0 and R_0 represent the capacitance and resistance of the electro-oxidation of adsorbed CO intermediates, respectively. Solid lines in Fig. 7 denote the corresponding fittings, where one can see that the fitting in general is very good. Fig. 8(c) depicts the variation of R_{CT} with electrode potentials at varied nanoparticle catalysts. It can be seen that the appearance of (pseudo)inductive characters (*i.e.*,

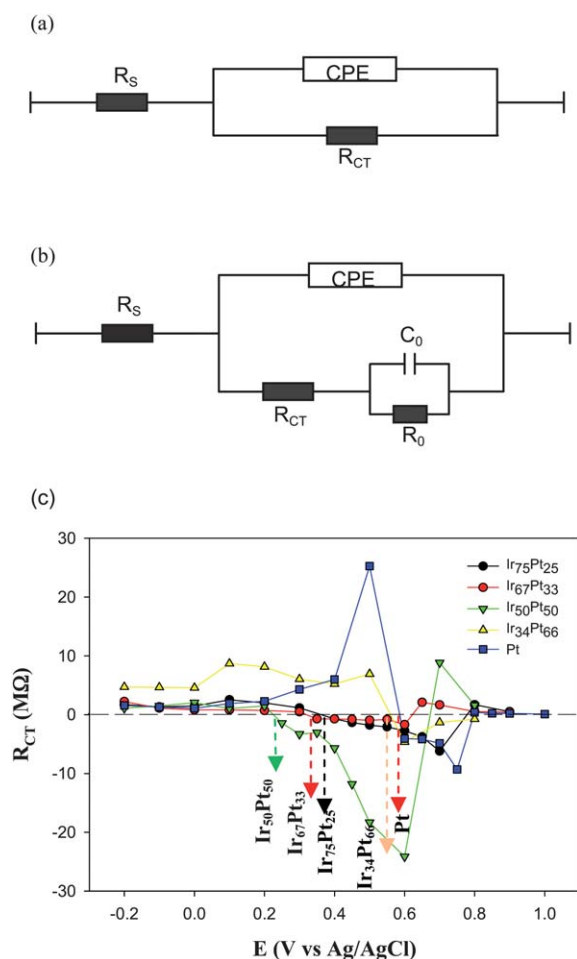


Fig. 8 Equivalent circuits for the electro-oxidation of formic acid at $\text{Ir}_x\text{Pt}_{100-x}/\text{Au}$ electrodes: (a) for normal impedance, and (b) for negative impedance shown in the Nyquist plots. R_{S} is the solution resistance, CPE (constant-phase element) and R_{CT} are the double-layer capacitance and charge-transfer resistance, respectively, and C_0 and R_0 represent the capacitance and resistance of the electro-oxidation of adsorbed CO intermediates. (c) Variation of R_{CT} with electrode potentials at different $\text{Ir}_x\text{Pt}_{100-x}/\text{Au}$ electrodes. Data are obtained by curve fitting of the impedance spectra (Fig. 7 and Fig. S2–S4†) by the equivalent circuits depicted in panels (a) and (b).

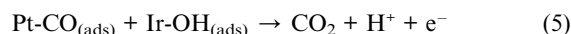
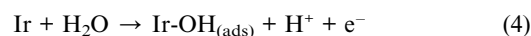
negative R_{CT}) coincided with the electro-oxidation of adsorbed poisonous CO species (Fig. 4). Therefore, the onset potentials of negative R_{CT} might be exploited to compare the tolerance to CO poisoning of the $\text{Ir}_x\text{Pt}_{100-x}$ nanoparticles. As indicated by the dashed arrows in Fig. 8, the onset potentials increase in the order of $\text{Ir}_{50}\text{Pt}_{50}$ (+0.23 V) < $\text{Ir}_{67}\text{Pt}_{33}$ (+0.32 V) < $\text{Ir}_{75}\text{Pt}_{25}$ (+0.36 V) < $\text{Ir}_{34}\text{Pt}_{66}$ (+0.55 V) < Pt (+0.59 V), which again shows that $\text{Ir}_{50}\text{Pt}_{50}$ represents the optimal composition among the series of nanoparticle catalysts.

Overall, the above measurements show that the electrocatalytic activities of $\text{Ir}_x\text{Pt}_{100-x}$ nanoparticles in formic acid oxidation varied significantly with the nanoparticle compositions, which can be interpreted on the basis of the bifunctional reaction mechanism.^{3,14–16} Note that the second metals in Pt-based alloys are generally believed to promote the removal of CO intermediates adsorbed on Pt sites by the formation of hydroxyl species on their surfaces.^{14,15,68} In the present study, formic acid electro-oxidation most likely follows a dual-pathway reaction mechanism, as proposed below:

Direct pathway



Indirect pathway



where the subscript “ads” denotes surface adsorbed species. It can be seen that in order to optimize the electrocatalytic performance of formic acid oxidation, the number of active Pt sites must be maximized for HCOOH adsorption and oxidation (eqn (1), direct pathway), and/or Ir surface sites are available for effective oxidative removal of poisonous CO intermediates by the formation of adsorbed hydroxyl species (eqn (2)–(5), indirect pathway). In the present $\text{Ir}_x\text{Pt}_{100-x}$ system, the particles with the Ir/Pt atomic ratio of 1 : 1 represents the optimal composition that exhibit the best electrocatalytic activity towards formic acid oxidation, as manifested in the voltammetric and impedance studies.

Conclusions

In this study, iridium-platinum alloy nanoparticles ($\text{Ir}_x\text{Pt}_{100-x}$) with tunable compositions were synthesized by thermolytic reduction of the corresponding salt precursors. The elemental composition of the resulting nanoparticles was determined by XPS measurements. HRTEM studies showed that the nanoparticles all exhibited well-defined crystalline structures with the average core diameters around 2 nm, regardless of the nanoparticle composition. The electrocatalytic activities of the $\text{Ir}_x\text{Pt}_{100-x}$ alloy nanoparticles towards formic acid oxidation were examined by voltammetric, chronoamperometric, and electrochemical impedance measurements in an acid electrolyte. Based on the current density of formic acid oxidation in the

anodic scan and the tolerance to CO poisoning, the catalytic performance was observed to strongly depend on the particle composition. Within the series, Ir₅₀Pt₅₀ nanoparticles were found to exhibit the best catalytic activity with the largest current density and the highest tolerance to CO poisoning, whereas Pt nanoparticles were heavily poisoned by CO adsorption with a low catalytic performance. Also, chronoamperometric measurements demonstrated that the Ir₅₀Pt₅₀ nanoparticles exhibited the maximum steady-state current density and long-term stability at different electrode potentials. In impedance measurements, negative impedance was observed at the potential windows where adsorbed CO intermediates were removed by electro-oxidation, in consistency with the presence of an inductive component. From the onset potential of negative impedance, Ir₅₀Pt₅₀ nanoparticles were found to exhibit the highest tolerance to CO poisoning. Taken together, these studies showed that the catalytic performance of the Ir_xPt_{100-x} alloy nanoparticles decreased in the sequence of Ir₅₀Pt₅₀ > Ir₆₇Pt₃₃ > Ir₇₅Pt₂₅ > Ir₃₄Pt₆₆ > Pt. That is, within the present experimental context, the IrPt alloy nanoparticles with the Ir/Pt atomic ratio of 1 : 1 represented the optimal composition towards formic acid oxidation.

Acknowledgements

This work was supported in part by the National Science Foundation (CHE-0718170/CHE-1012258 and CHE-0832605). XPS and TEM work was carried out at the Molecular Foundry and National Center for Electron Microscopy, Lawrence Berkeley National Laboratory, which is supported by the US Department of Energy.

Notes and references

- B. C. H. Steele and A. Heinzl, *Nature*, 2001, **414**, 345–352.
- R. A. Lemons, *J. Power Sources*, 1990, **29**, 251–264.
- S. Wasmus and A. Kuver, *J. Electroanal. Chem.*, 1999, **461**, 14–31.
- J. Willsau and J. Heitbaum, *Electrochim. Acta*, 1986, **31**, 943–948.
- C. Rice, R. I. Ha, R. I. Masel, P. Waszczuk, A. Wieckowski and T. Barnard, *J. Power Sources*, 2002, **111**, 83–89.
- Y. M. Zhu, S. Y. Ha and R. I. Masel, *J. Power Sources*, 2004, **130**, 8–14.
- A. C. Chen and P. Holt-Hindle, *Chem. Rev.*, 2010, **110**, 3767–3804.
- W. Chen, J. Kim, S. H. Sun and S. W. Chen, *Phys. Chem. Chem. Phys.*, 2006, **8**, 2779–2786.
- Y. C. Lu, Z. C. Xu, H. A. Gasteiger, S. Chen, K. Hamad-Schifferli and Y. Shao-Horn, *J. Am. Chem. Soc.*, 2010, **132**, 12170–12171.
- N. Tian, Z. Y. Zhou, S. G. Sun, Y. Ding and Z. L. Wang, *Science*, 2007, **316**, 732–735.
- W. Chen, J. M. Kim, L. P. Xu, S. H. Sun and S. W. Chen, *J. Phys. Chem. C*, 2007, **111**, 13452–13459.
- Y. X. Chen, A. Miki, S. Ye, H. Sakai and M. Osawa, *J. Am. Chem. Soc.*, 2003, **125**, 3680–3681.
- H. Shiroishi, Y. Ayato, K. Kunimatsu and T. Okada, *J. Electroanal. Chem.*, 2005, **581**, 132–138.
- M. T. M. Koper, J. J. Lukkien, A. P. J. Jansen and R. A. van Santen, *J. Phys. Chem. B*, 1999, **103**, 5522–5529.
- T. Iwasita, *Electrochim. Acta*, 2002, **47**, 3663–3674.
- H. Igarashi, T. Fujino, Y. M. Zhu, H. Uchida and M. Watanabe, *Phys. Chem. Chem. Phys.*, 2001, **3**, 306–314.
- J. Y. Chen, B. Lim, E. P. Lee and Y. N. Xia, *Nano Today*, 2009, **4**, 81–95.
- J. Y. Park, Y. Zhang, M. Grass, T. Zhang and G. A. Somorjai, *Nano Lett.*, 2008, **8**, 673–677.
- G. A. Somorjai and J. Y. Park, *Top. Catal.*, 2008, **49**, 126–135.
- W. Chen, L. P. Xu and S. W. Chen, *J. Electroanal. Chem.*, 2009, **631**, 36–42.
- Y. Z. Lu and W. Chen, *Chem. Commun.*, 2011, **47**, 2541–2543.
- S. Zhang, Y. Y. Shao, H. G. Liao, J. Liu, I. A. Aksay, G. P. Yin and Y. H. Lin, *Chem. Mater.*, 2011, **23**, 1079–1081.
- H. Zhao, J. Yang, L. Wang, C. G. Tian, B. J. Jiang and H. G. Fu, *Chem. Commun.*, 2011, **47**, 2014–2016.
- B. M. Leonard, Q. Zhou, D. N. Wu and F. J. DiSalvo, *Chem. Mater.*, 2011, **23**, 1136–1146.
- J. S. Huang, H. Q. Hou and T. Y. You, *Electrochem. Commun.*, 2009, **11**, 1281–1284.
- U. A. Paulus, A. Wokaun, G. G. Scherer, T. J. Schmidt, V. Stamenkovic, N. M. Markovic and P. N. Ross, *Electrochim. Acta*, 2002, **47**, 3787–3798.
- W. J. Zhou and J. Y. Lee, *J. Phys. Chem. C*, 2008, **112**, 3789–3793.
- W. P. Zhou, A. Lewera, R. Larsen, R. I. Masel, P. S. Bagus and A. Wieckowski, *J. Phys. Chem. B*, 2006, **110**, 13393–13398.
- W. Chen and S. W. Chen, *Angew. Chem., Int. Ed.*, 2009, **48**, 4386–4389.
- F. Maillard, M. Eikerling, O. V. Cherstiouk, S. Schreiber, E. Savinova and U. Stimming, *Faraday Discuss.*, 2004, **125**, 357–377.
- W. Chen, J. M. Kim, S. H. Sun and S. W. Chen, *Langmuir*, 2007, **23**, 11303–11310.
- H. N. Dinh, X. M. Ren, F. H. Garzon, P. Zelenay and S. Gottesfeld, *J. Electroanal. Chem.*, 2000, **491**, 222–233.
- M. Watanabe, M. Uchida and S. Motoo, *J. Electroanal. Chem.*, 1987, **229**, 395–406.
- Y. Lin and R. G. Finke, *Inorg. Chem.*, 1994, **33**, 4891–4910.
- J. Dupont, G. S. Fonseca, A. P. Umpierre, P. F. P. Fichtner and S. R. Teixeira, *J. Am. Chem. Soc.*, 2002, **124**, 4228–4229.
- G. S. Fonseca, A. P. Umpierre, P. F. P. Fichtner, S. R. Teixeira and J. Dupont, *Chem.–Eur. J.*, 2003, **9**, 3263–3269.
- A. Aramata, T. Yamazaki, K. Kunimatsu and M. Enyo, *J. Phys. Chem.*, 1987, **91**, 2309–2314.
- M. M. Hefny and S. AbdelWanees, *Electrochim. Acta*, 1996, **41**, 1419–1422.
- X. W. Yu and P. G. Pickup, *J. Power Sources*, 2008, **182**, 124–132.
- H. Tsapraillis and V. I. Birss, *Electrochem. Solid-State Lett.*, 2004, **7**, A348–a352.
- P. Sivakumar and V. Tricoli, *Electrochem. Solid-State Lett.*, 2006, **9**, A167–a170.
- A. C. Chen, D. J. La Russa and B. Miller, *Langmuir*, 2004, **20**, 9695–9702.
- Q. F. Yi, A. C. Chen, W. Huang, J. J. Zhang, X. P. Liu, G. R. Xu and Z. H. Zhou, *Electrochem. Commun.*, 2007, **9**, 1513–1518.
- C. C. Shan, D. S. Tsai, Y. S. Huang, S. H. Jian and C. L. Cheng, *Chem. Mater.*, 2007, **19**, 424–431.
- K. Ohyama, T. Sugino, T. Nitta, C. Kimura and H. Aoki, *Electrical Engineering in Japan*, 2011, **174**, 45–50.
- H. Y. Jung, S. Park, P. Ganesan and B. N. Popov, *Proton Exchange Membrane Fuel Cells 8, Pts 1 and 2*, 2008, **16**, 1117–1121.
- H. Y. Jung, S. Park and B. N. Popov, *J. Power Sources*, 2009, **191**, 357–361.
- T. Ioroi and K. Yasuda, *J. Electrochem. Soc.*, 2005, **152**, A1917–A1924.
- K. I. B. Eguluz, G. R. Salazar-Banda, D. Miwa, S. A. S. Machado and L. A. Avaca, *J. Power Sources*, 2008, **179**, 42–49.
- W. Chen, J. R. Davies, D. Ghosh, M. C. Tong, J. P. Konopelski and S. W. Chen, *Chem. Mater.*, 2006, **18**, 5253–5259.
- W. Chen, S. W. Chen, F. Z. Ding, H. B. Wang, L. E. Brown and J. P. Konopelski, *J. Am. Chem. Soc.*, 2008, **130**, 12156–12162.
- N. Chakroune, G. Viau, S. Ammar, L. Poul, D. Veautier, M. M. Chehimi, C. Mangeney, F. Villain and F. Fievet, *Langmuir*, 2005, **21**, 6788–6796.
- G. Viau, R. Brayner, L. Poul, N. Chakroune, E. Lacaze, F. Fievet-Vincent and F. Fievet, *Chem. Mater.*, 2003, **15**, 486–494.
- D. J. Davis, G. Kyriakou and R. M. Lambert, *J. Phys. Chem. B*, 2006, **110**, 11958–11961.
- J. F. Moulder, W. F. Stickle, P. E. Sobol and K. D. Bomben, Physical Electronics, Inc., Eden Prairie, MN, 1995.
- J. P. Wang, P. Holt-Hindle, D. MacDonald, D. F. Thomas and A. C. Chen, *Electrochim. Acta*, 2008, **53**, 6944–6952.
- J. B. Xu, T. S. Zhao and Z. X. Liang, *J. Phys. Chem. C*, 2008, **112**, 17362–17367.
- J. H. Zeng, J. Yang, J. Y. Lee and W. J. Zhou, *J. Phys. Chem. B*, 2006, **110**, 24606–24611.

-
- 59 J. A. Creighton and D. G. Eadon, *J. Chem. Soc., Faraday Trans.*, 1991, **87**, 3881–3891.
- 60 H. Andreas, H. Elzanowska, I. Serebrennikova and V. Birss, *J. Electrochem. Soc.*, 2000, **147**, 4598–4604.
- 61 V. I. Birss, H. Andreas, I. Serebrennikova and H. Elzanowska, *Electrochem. Solid-State Lett.*, 1999, **2**, 326–329.
- 62 T. Toda, H. Igarashi, H. Uchida and M. Watanabe, *J. Electrochem. Soc.*, 1999, **146**, 3750–3756.
- 63 Y. Xu, A. V. Ruban and M. Mavrikakis, *J. Am. Chem. Soc.*, 2004, **126**, 4717–4725.
- 64 M. Watanabe, K. Tsurumi, T. Mizukami, T. Nakamura and P. Stonehart, *J. Electrochem. Soc.*, 1994, **141**, 2659–2668.
- 65 I. M. Hsing, X. Wang and Y. J. Leng, *J. Electrochem. Soc.*, 2002, **149**, A615–a621.
- 66 E. P. Lee, Z. M. Peng, W. Chen, S. W. Chen, H. Yang and Y. N. Xia, *ACS Nano*, 2008, **2**, 2167–2173.
- 67 Q. G. He, W. Chen, S. Mukerjee, S. W. Chen and F. Laufek, *J. Power Sources*, 2009, **187**, 298–304.
- 68 H. A. Gasteiger, N. Markovic, P. N. Ross and E. J. Cairns, *J. Phys. Chem.*, 1993, **97**, 12020–12029.